RESEARCH PAPER

Spatter formation in laser beam welding using laser beam oscillation

**Florian Hugger · Konstantin Hofmann · Stefanie Kohl ·
Michael Dobler · Michael Schmidt**

Abstract This paper presents an approach towards a better
understanding of spatter formation in laser beam welding.
Hereunto, experimental investigations and numerical simula-
tion are carried out. For the study, various steels and alumin-
ium alloys were selected to investigate the influences of
alloying elements upon spatter formation. The welding was
performed by applying a laser beam oscillation technique in
which weld seam is generated by a spiral movement of the
laser beam, in order to check the influence of weld pool
movement according to spatter formation. This strategy was
also transferred to the numerical simulation to get a detailed
insight into the processes taking place in the keyhole when
spatters form. Furthermore, a new detection method is pre-
sented which allows a three-dimensional tracking of spatters
by using a pair of synchronised stereo cameras.

F. Hugger · K. Hofmann (✉)
Bayerisches Laserzentrum GmbH, Erlangen, Germany
e-mail: k.hofmann@blz.org

F. Hugger
e-mail: f.hugger@blz.org

S. Kohl · M. Dobler · M. Schmidt
Photonic Technologies, University of Erlangen-Nuremberg, SAOT,
Erlangen, Germany

S. Kohl
e-mail: stefanie.kohl@lpt.uni-erlangen.de

M. Dobler
e-mail: michael.dobler@lpt.uni-erlangen.de

M. Schmidt
e-mail: michael.schmidt@lpt.uni-erlangen.de

1 Introduction

Production industry still suffers from inflexible manufacturing
systems. Up to date in an assembly of different parts for every
single weld joint an appropriate welding process has to be
provided, since the demands of material thickness, welding
gap, joint configuration and furthermore have to be taken into
account. If the steadily increasing process requirements are
still rising, every joint lacks an own production line with a
suitable laser source and optics.

Nevertheless, the development of high brightness laser
sources in combination with fast galvanometer scanning sys-
tems offers a solution to integrate different joints in a single
production line. The combined system performs fast machin-
ing speed due to high energy densities on the surface and
flexible seam forming due to an arbitrary line movement [1].
Therefore, both penetration depth and weld bead width can be
adapted to specific requirements [2]. A general expression of
the line movement of the laser spot in x and y direction is given
in Eqs. (1) and (2). The x direction denominates the primary
welding direction and y denominates perpendicular direction
to the welding direction.

$$x(t) = x_0 + v * t + a * \sin(2\pi * f_x * t + \phi_x) \quad (1)$$

$$y(t) = y_0 + b * \sin\left(2\pi * f_y * t + \phi_y\right) \quad (2)$$

Where $x(t)$ and $y(t)$ are the time-dependent coordinates; x_0
and y_0 are the start position; v is the welding speed; t is the
time; a and b are the oscillation amplitudes; f_x and f_y are the
oscillating frequencies Φ_x and Φ_y are the phase angles at the
beginning of the oscillating movement.

Thus, arbitrary seam geometries can be formed [3]. Most
common shapes of the beam movement are circles or helixes
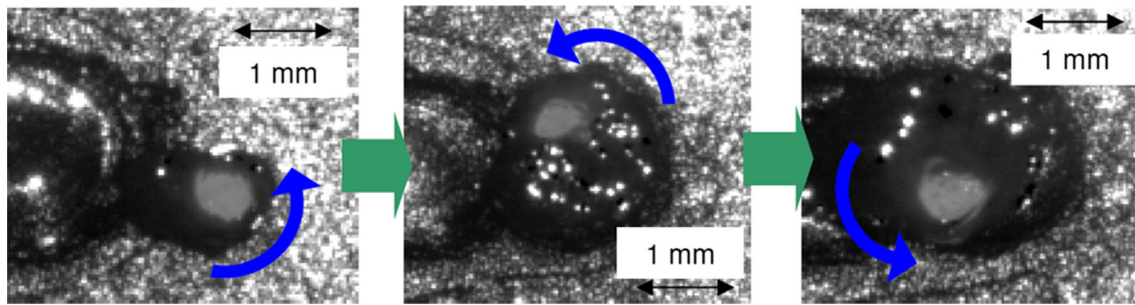against the background to broaden the weld seam for gap

Fig. 1 Illustration of the beam oscillation. Steel; 3 kW; 0.05 m/s; 600 μm focus diameter; left, process at 0 ms; middle, process at 0.08 s; right, process at 0.16 s; frame rate=1,000 fps; resolution, 1,280×208

bridging, to improve weld seam appearance when welding zinc coated sheets or to improve the intermixture of dissimilar materials [1, 3, 4]. An example of a circular laser beam movement is displayed in Fig. 1. The keyhole is generated and moves along a circular path (left panel). After three-quarter of a turn, the capillary enters the spreading melt pool (middle panel). For the last quarter, the keyhole moves within already molten material (right panel).

Compared to a linear movement of the laser spot, a larger cross section area is melted by using the beam oscillation. Consequently, for producing equal cross section areas compared to linear movement, a downsizing of the laser source power is possible. Furthermore, researchers report a significant improvement of the welding process stability and a reduction of pores when welding aluminium alloys [5]. Dependent upon the welding strategy forming of pores and spatter increases or decreases compared to a conventional deep welding [1]. Besides these advantages, the process shows a significant amount of spatter formation when certain parameter combinations are applied [6]. From analysis of the process of steel welding processes, it can be seen that spatter is formed mostly at the keyhole rim at the front side of the

keyhole (Fig. 2). Subsequently, for reasons of the dimensioning of spatter deflection systems and for a better understanding of the processes in laser beam welding, the formation mechanisms have to be investigated.

2 Principles of spatter formation in laser beam welding

Due to the impact of the laser beam, the material in the interaction zone is melted and vaporized. In the keyhole, vapour streams out with several hundred meters per seconds [7]. Depending upon the welding regime different appearances of spatter occur [8, 9]. Below a welding speed $v_w<0.08$ m/s, a chaotic spatter formation can be observed, where the particles have no predominant direction, see Fig. 3.

This behaviour is attributed to random evaporation on the keyhole surface, which is locally increased at the bottom of the keyhole. The keyhole itself has a low inclination angle in feeding direction. Increasing the welding speed v_w above $v_w<0.08$ m/s the inclination angle of the keyhole also increases, which leads to a predominant ejection of spatter against the feeding direction. Due to an enforced vapour jet towards the
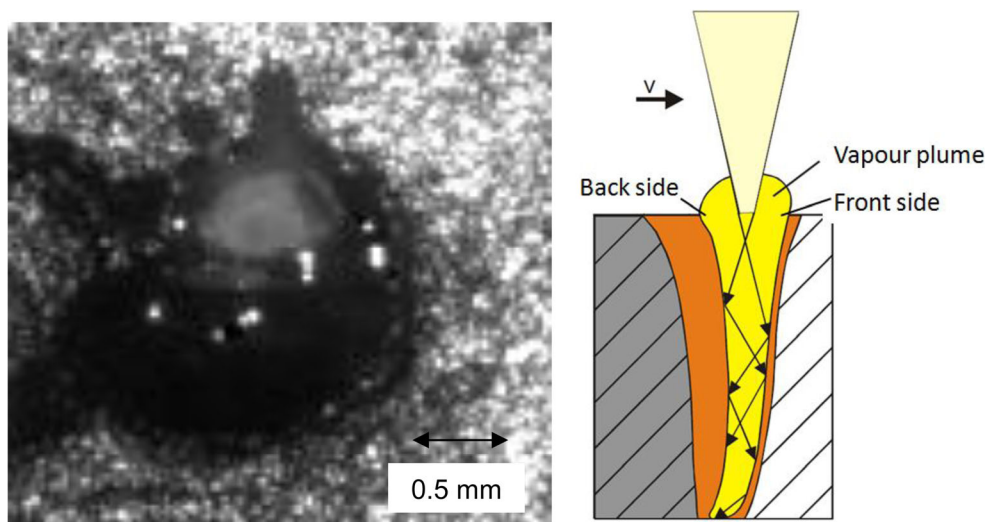

Fig. 2 Spatter formation during laser beam oscillation welding; left, Steel; disc laser; 3 kW; 0.05 m/s; 600 μm focus diameter; frame rate=1,000 fps; resolution 1,280×208; right, schematic drawing of keyhole
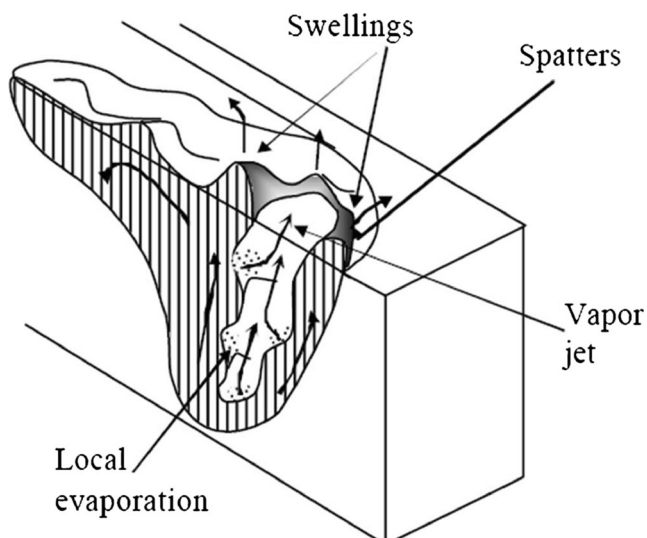
Fig. 3 Spatter formation in the keyhole [8]

rear wall of the keyhole, caused by a dominant evaporation at the keyhole front or caused by volatile alloying elements or coatings [10], particles are separated from the melt pool [9]. The occurrence of spatter can be classified considering the

emergence, separation location and conditions of the particles [11]. Regarding spatter size and velocity, it is reported in [9] that the size is decreasing with increasing welding speed. Investigations of spatter size and velocity during laser welding of aluminium alloy with different laser sources show an average particle velocity of 0.75 m/s and an average spatter size of 0.2 mm for a CO_2-laser and 3 m/s and 0.13 mm for a fibre laser, respectively [12]. The origin of ejected particles is also connected to burning alloying elements [13]. That is, carbon reacts with oxygen from atmosphere which leads to ejections.

Though the emergence of spatter is well known, physical mechanisms which define size and the velocity of the particles are not investigated. Consequently, this paper shall provide a first step towards a better understanding of the basic mechanism,

3 Experimental and numerical setup

3.1 Experimental setup

The experiments are carried out using a 1 kW fibre laser with a wavelength of 1,070 nm and $M^2 < 1.1$. For the investigations,
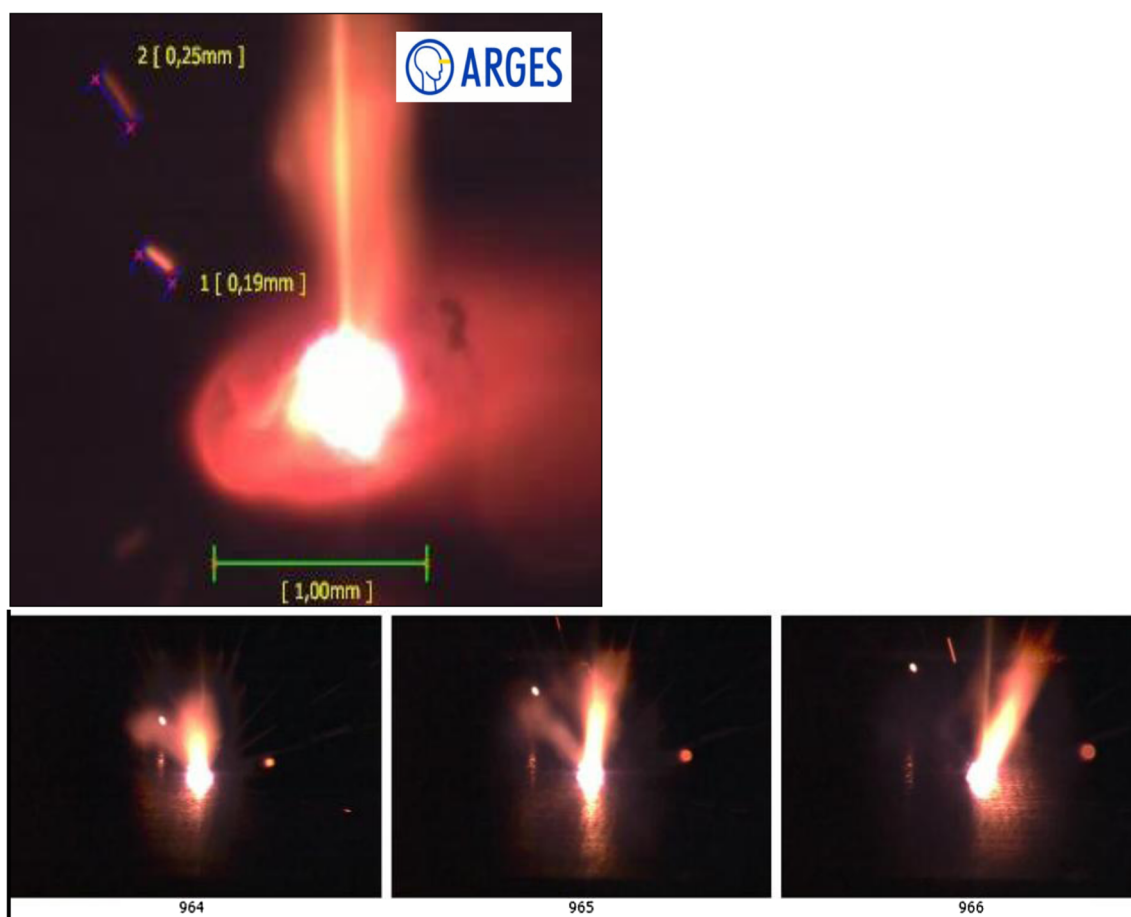

Fig. 4 Automated measurement of particle size during welding of Al99.5 using the software motion analyser; 680 W; 0.02 m/s; 50 μm focus diameter; frame rate=6,000 fps

the laser power is set to 680 W. The laser beam is guided by a mode optical fibre with a diameter of 45 μm to a 3D scanning system *welding elephant* from *ARGES*, which focuses the beam to a spot diameter of 80 μm. For the detection of material ejections, a high-speed-camera was applied.

The CMOS-camera has a maximum technical frame rate of 230.000 frames per second at a resolution of 160×32. The determination of the velocity was carried out using a corresponding software tool *motion graph*, which is tracing the particles and its position change between two frames. In Fig. 4, an automatically measurement of the size of two particles and the keyhole diameter is shown. Only particles are taken into account, whose flight paths are in the focus plain of the camera, which means only spatter perpendicular to the viewing direction of the camera is analysed. Furthermore, the total number of particles are counted and divided through the seam length to get the average number per millimeter.

For the investigation of the dependency of spatter formation from materials and composition, two steels and three aluminium alloys are tested in order to check the influence of alloying elements and different vapour plumes in dependence of different material thicknesses to the spatter velocity, whereat ten spatters for each material have been appraised. The materials are listed in Table 1. In the welding experiments, V2A and Dispal are one partly penetrated due to their material thickness of 10 and 25 mm, while the other materials are fully penetrated with a material thickness of 1 mm. Spatter formation was only detected on the upper exit of the keyhole, since the lower exit was inaccessible for optical detections.

The movement of the laser beam is designed to a helix shape. The scanning speed was set to 0.02 m/s, the oscillation frequency to 200 Hz and the amplitude of 0.5 mm was applied. The resulting movement of the laser spot is displayed in Fig. 5.

3.2 Numerical setup

Besides experimental investigations, numerical simulations are carried out, using a three-dimensional transient simulation model for laser-based material processing. The used model has been described in detail in [14, 15] and comprises heat
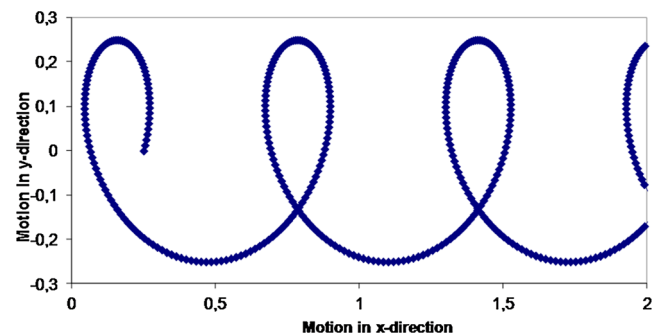

Fig. 5 Movement of the laser beam

conduction due to the angle-dependent absorption and multiple reflections of the laser beam and phase transitions of the metal. The fluid dynamics include vapor pressure, surface tension and viscosity. Since there is a lack of literature for consistent sets of thermo-mechanic and fluid-dynamic properties of alloys in the temperature range up to evaporation, these were substituted with those of pure iron and aluminum in the simulations. The parameters used are equal to the experimental investigation.

4 Results and discussion

4.1 Experimental results

A comparison of the two aluminium alloys AlMg3 and Al99.5 which were fully penetrated shows a different behaviour in spatter formation. The average measured velocity of the particles is 0.5 m/s, and the number of particles per volume weld seam is 24 1/mm³ when welding AlMg3 and 2 m/s and 2 1/mm³ when welding Al99.5. This behaviour can be explained by the influence of volatile magnesium in the melt which leads to a higher evaporation rate due to a high vapour pressure [16] and consequently an increased amount of entrained particles.
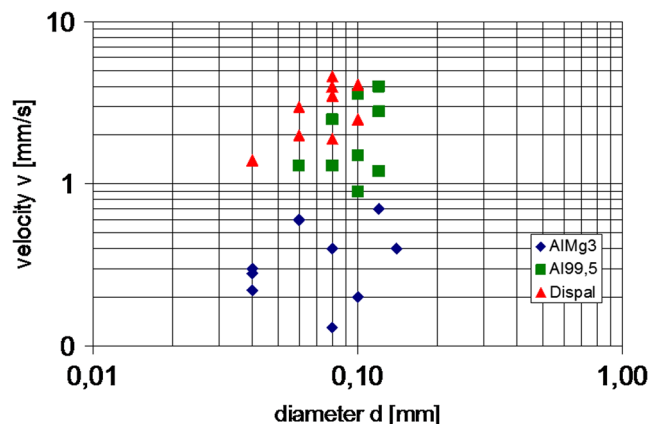

Fig. 6 Size and velocity distribution of tracked spatters of aluminium alloys

Table 1 Steel and aluminium materials and their corresponding thicknesses

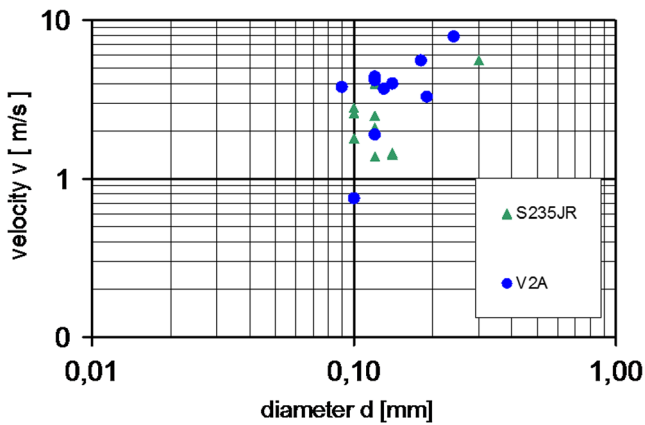| Steels	Aluminium alloys
X2CrNiMo1810	AlSi35
(V2A)	(Dispal)
10 mm	25 mm
S235JR	Al99,5
1 mm	1 mm
	AlMg3
	1 mm

Fig. 7 Size and velocity distribution of tracked spatters of steels

Dispal shows equal particle sizes as AlMg3 and Al99.5, but the spatter velocity exceeds the velocity of Al99.5 with an average of 3 m/s. This may be a result of the increased penetration depth of 1.5 mm which increases the vapour velocity in the keyhole. In Fig. 6, the experimental results of measured spatter sizes (nine of each material) and velocities for aluminium alloys are displayed.

Spatter generated during welding of V2A and S235 shows for both materials higher average velocities and an increased average volume of particles compared to aluminium. The number of particles per volume is 8 and 2 1/mm³ at V2A and S235, respectively. In Fig. 7, the experimental results of measured spatter sizes and velocities for steels are displayed.

4.2 Numerical simulation

In Fig. 8, the simulation, which was done in OpenFOAM®, of the detachment of a droplet in iron can be observed. The figure shows a cross-section through the keyhole perpendicular to the laser feed. To simplify the images, only the boundary

between metal and air is visualized, but not the metal itself. The pixel-like structure of the images is due to the spatial discretization of the simulation to reduce process time. In panel a, the keyhole and the upper and lower surface of the metal sheet can be seen. The following panels show magnifications of the top side of the keyhole and are given in chronological order. In panel b, a small hump rises at the keyhole top. This hump grows further, as given in panel c, until an aspect ratio of more than one is reached (panel d). Then, surface tension leads to the contraction of the neck of the hump until a droplet forms and detaches (panel e). Due to the impulse of the melt, the droplet takes off to the top (panel f and g).

Figure 9 shows the detachment process of droplets in aluminium. The cross-section, the visualization and the order of the panels are identical to those of the images before. Though here, the lower viscosity causes the melt to be more dynamic. This leads not only to droplet formation, but also to a more dynamic keyhole, as can be taken also from the figure. The detachment follows the same process scheme as in Fig. 8. Again, a hump at the top of the keyhole forms (panel b–d) until a certain aspect ratio is attained (panel e). Then, the neck of the elevation contracts again and a droplet detaches (panel e and f). However, in panel f, it can be seen that the droplet did not detach at the bottom of the elevation and thus, a melt hump remains after the detachment. This leads to a second detachment of a droplet (panel g–i) directly following the first detachment.

5 Discussion

Both the experiments and the numerical simulation show a formation of spatter at the rim of the keyhole where humps are
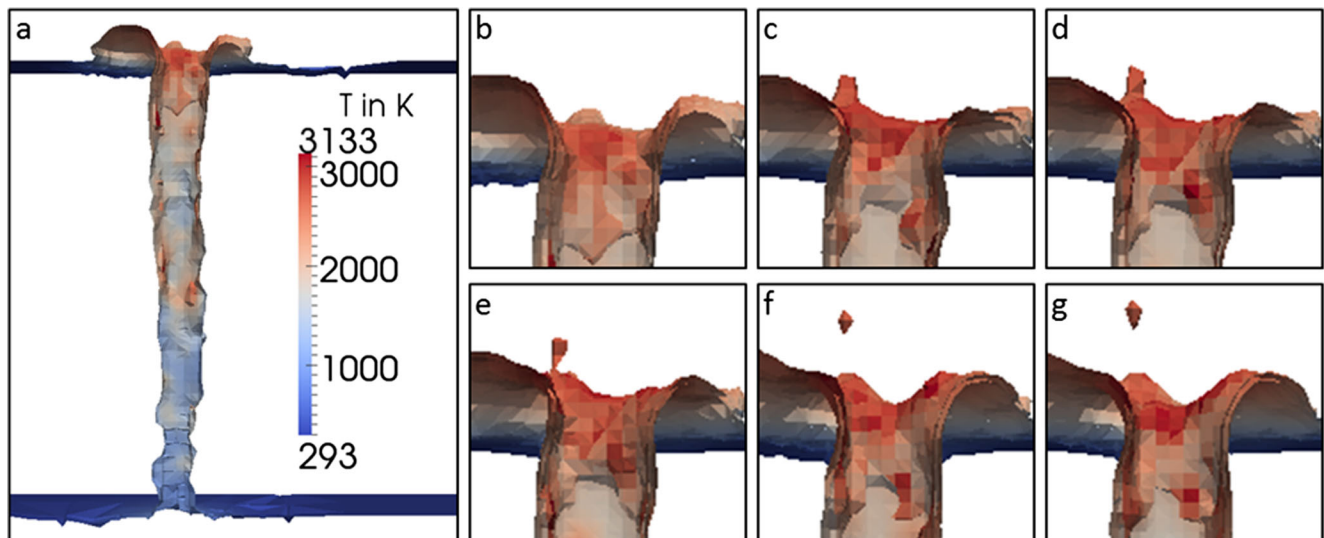

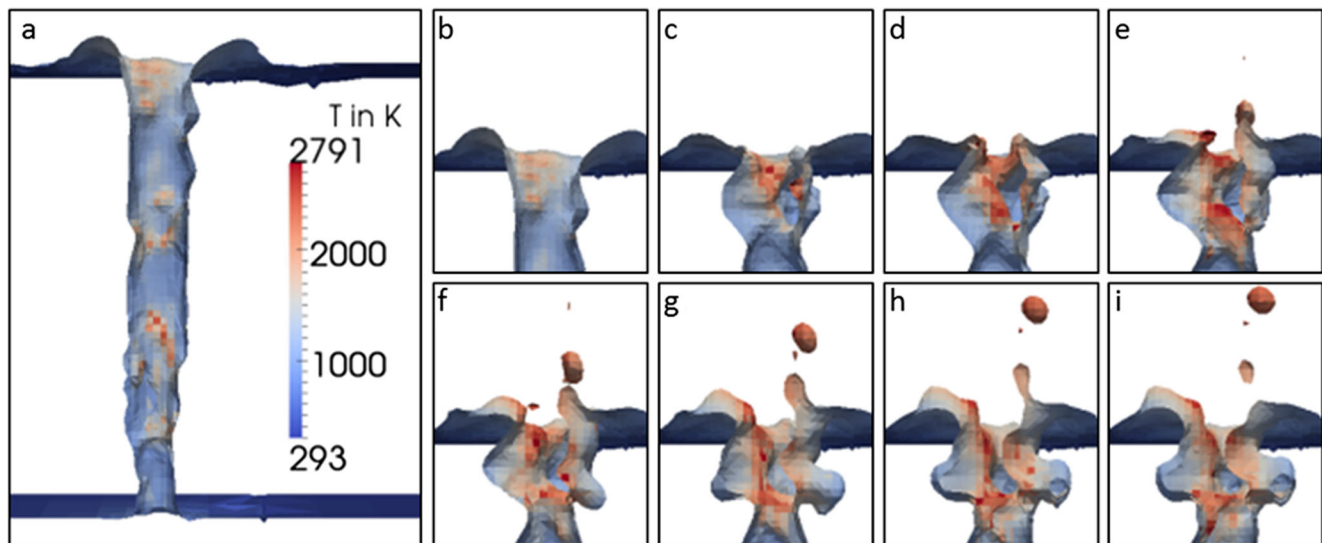Fig. 8 Metal-air interface of a cross-section through a keyhole for iron

Fig. 9 Metal-air interface of a cross-section through a keyhole for aluminum

formed and particles are detached from the melt pool. Moreover, the investigations display the formation of different particle sizes and velocities which are entrained at the rim of the keyhole and are not generated by resonant surface waves like observed in [9]. Summing up, experimental and simulative results fit well. For a more general view on spatter formation in laser beam welding, the processes taking place at the keyhole rim can be described as a disintegration process into single particles. Here, the metal vapour is the streaming medium acting against the surface tension of the melt. For the description of the atomization, the characteristic Reynolds number is used, which describes the ratio of inertia forces to viscous forces and the Ohnesorge number, as a measure of viscous forces to inertia forces and surface tension. The numbers can be calculated as given in Eqs. (3) and (4):

$$Oh = \frac{\eta_m}{\sqrt{\sigma_m \rho_m d_s}} \qquad (3)$$

$$Re = \frac{v_v d_k}{\mu_v} \qquad (4)$$

Where Oh is the Ohnesorge number; Re is the Reynolds number; η_m is the melt dynamic viscosity; σ_m i the melt surface tension; ρ_v is the vapour density; ρ_m is the melt density; μ_v is the vapour kinematic viscosity; v_v is the vapour velocity; d_s is the spatter diameter and d_k is the dimension of the keyhole.

Since exact properties of liquid metals at evaporation temperature are not available, appraised values for aluminium are ρ_m=2,300 kg/m^3, η_m=10^{-3} Pa*s, σ_m=0.1 N/m, v_v=10 m/s, μ_v=0.1^{-4} m^2/s, ρ_v=0.5 kg/m^3, d_s=0.1 mm and d_k=0.5 mm. This leads to values of $Oh \approx 10^{-4}$ and $Re \approx 10^5$. For steel, the

values are in the same dimension. Both values can be merged in the so called Ohnesorge diagram, see Fig. 10.

From the calculated values, Oh and Re can be drawn that the spatter formation in laser welding is basically a corrugating effect. This is confirmed by high speed imaging of the process (see Fig. 2), in which the formation of humps at the keyhole rim can be observed that are elongated and finally separated from the melt pool.

Though there are differences in spatter size and velocity for varying materials and alloys, further experiments have to be carried out to correlate spatter formation and material properties like surface tension and melt viscosity. Moreover, it is still unsolved how particle size and number per volume are interconnected to get an understanding of how both can be influenced and if they can be influenced separately. Consequently, more detailed investigations have to be carried out regarding the effects of penetration depth and alloying elements. Furthermore, the transitions of the different disintegration regimes have to be adapted to the laser welding process since the
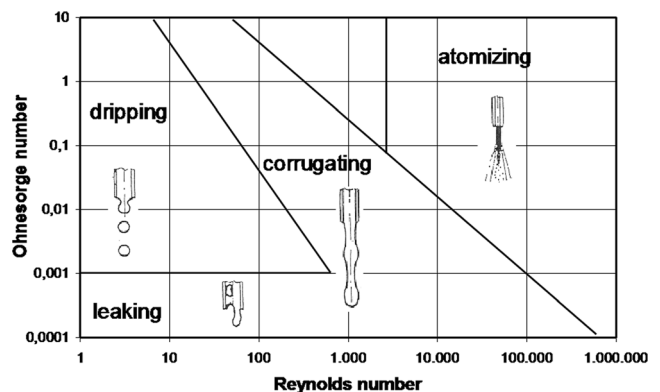

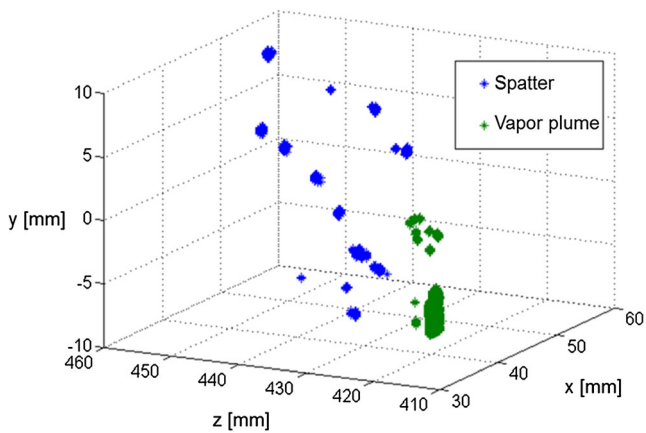**Fig. 10** Dispersions phenomena of liquids [17]

Fig. 11 Three-dimensional visualization of welding spatter and vapour plume. V2A; 3 kW; 0.12 m/s; 600 μm focus diameter

particles are entrained from a curved surface instead of a liquid jet like ideally assumed.

6 Developments in spatter detection

The 2D imaging of the welding process limits the tracking of size and velocity of spatters to the focal area with a perpendicular trajectory to the viewing direction of the camera and consequently the majority of the spatters cannot be taken into account. Nevertheless, high speed camera process observation not only provides conventional two-dimensional visualization of the welding process dynamics, but can also be used to derive detailed three-dimensional information about spatter

formation. This is possible by using a setup with a pair of synchronized stereo cameras that are recording the same scene from different points of view. By performing an accurate stereo calibration of the camera system and applying stereo vision algorithms to pairs of images, depth information can be retrieved from the combined 2D information of both cameras. This makes a three-dimensional visualization of vapor plum and spatters possible.

In the experiments, two cameras with 100 kHz frame rate at a resolution of 256×208 pixels to record the image data have been used. All results shown are based on welding with power of 3,000 W and a welding velocity of 0.11 m/s. To obtain three-dimensional data, a stereo algorithm based on the graph cut technique [18] was applied to each pair of images. These results are visualized in Fig. 11.

Both the vapor plume (green) formed in the welding process and various spatters (blue) are depicted. Thereby, for each object, its position and shape in space could be reconstructed. Stereo imaging not only allows determining the position and distribution of spatter in space but also makes it possible to analyze the movement of the spatter in three-dimensions. To do this, an algorithm was developed which recognizes each droplet in the subsequent image pairs and thus allows tracking of the movement of each detected spatter over time. The results of such a calculation for a sequence of 100 images showing five particles are given in Fig. 12.

The reconstruction of the spatter movement as smooth trajectories without significant noise demonstrates the high accuracy of the applied algorithms. The derived information can be used to automatically determine various properties of

Fig. 12 Three-dimensional visualization of spatter droplet movement. Welding was performed in +z-direction
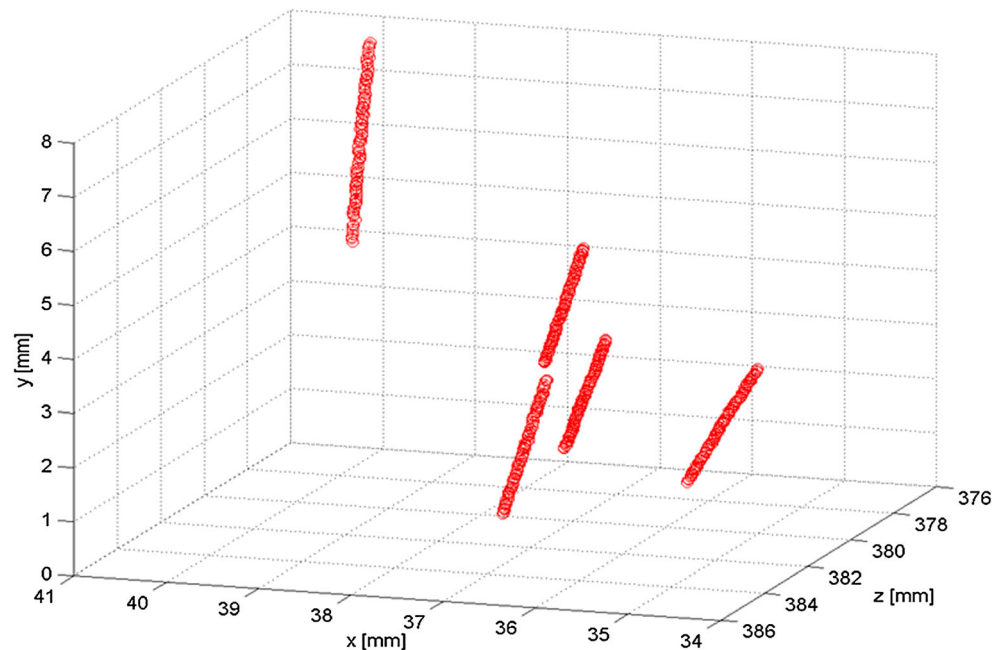
the spatter movement. For example, the angle of spatter movement relative to the sheet metal plane in Fig. 11 is 40.5°. Of course, the reconstructed trajectories can also be used to calculate three-dimensional velocities of the spatter. For example, the average velocity of the spatter in the image sequence analyzed in Fig. 11 was calculated to be 2.95 m/s.

Coming investigations will validate the method regarding the detection of particle size by using high-melting tungsten carbide of known particle size. In the future, the stereo setup and the developed algorithms will offer great potential to perform detailed investigations of spatter movement with higher accuracy than it was possible with single camera imaging. By a close-up imaging of the process zone, this technique also offers the perspective to perform 3D visualization of spatter formation which provides the opportunity to improve spatter deflection by adaptable systems, i.e., automated cross jets.

7 Conclusion and outlook

The formation of spatter during laser welding was investigated experimentally by high-speed imaging and modelled by numerical simulation. Both methods showed particle ejection at the keyhole rim where a hump is formed which is subsequently separated form the melt. From the investigation of different materials, similar particle sizes and velocities were determined at which only slight differences occur. By calculation of the Ohnesorge number and the Reynolds number, the process is described as corrugating connecting the process to disintegration regimes. In principle, this allows determining the particle generation by knowledge of the material properties or calculating, i.e., the vapour velocity.

Due to the limitations of particle tracking only perpendicular to the viewing direction, a method was developed to enable a 3D detection of the process by adding a second stereo high-speed camera. Consequently, it is possible to calculate the 3D trajectories of ejected particles and to take all generated particles into account for measurement, i.e., for the use of developing systems for particle deflection.

Future investigations will take a more detailed look into the spatter formation depending upon the penetration depth, welding speed and alloy composition. Here, the changing of disintegration regimes should be determined and thus the applicability of the theory of disintegration shall be confirmed and extended.

References

1. Schmitt F (2012) Laserstrahl-Mikroschweißen mit Strahlquellen hoher Brillanz und örtlicher Leistungsmodulation. Dissertation RWTH Aachen, Shaker Verlag GmbH – Laser beam micro welding using high brilliant laser sources and local power modulation
2. Schweier M, Hatwig J, Zaeh MF, Reppich J (2011) Single mode fiber beam welding with superposed beam oszillations. In Proceedings of the ICALEO, pp 536–546
3. Mahrle A, Beyer E (2007) Control of the energy deposition during laser beam welding by oscillation techniques. In: Proceedings of Lasers in Manufacturing, pp. 97–104
4. Kraetsch M, Standfuss J, Klotzbach A, Kaspar J, Brenner B, Beyer E (2011) Laser beam welding with high-frequency beam oscillation: welding of dissimilar materials with brilliant fiber lasers. In: Lasers in Manufacturing, pp. 142–149
5. Meier O (2006) Hochfrequentes Strahlpendeln zur Erhöhung der Prozessstabilität mit hoher Schmelzbaddynamik. AiF-final report of project 13600 N, High frequency beam oscillation for increased process robustness with high weld pool dynamics
6. Schweier M, Heins JF, Haubold MW, Zaeh MF (2013) Spatter formation in laser welding with beam oscillation, Proceedings of Laser in Manufacturing, pp. 20–30
7. Funk M (1994) Absorption von CO2-Laserstrahlung beim Laserstrahlschweißen von Grobblech. Dissertation RWTH Aachen, Shaker Verlag GmbH, Absorption of CO2 laser radiation at laser beam welding of thick plates
8. Fabbro R, Silami S (2007) Melt pool dynamics during deep penetration cw Nd-Yag laser welding. In: Proceedings of Lasers in Manufacturing, pp. 259–264
9. Weberpals J.-P (2010) Nutzen und Grenzen guter Fokussierbarkeit beim Laserschweißen. Dissertation of IFSW, Stuttgart, Benefits and limits of strong focusability at laser welding
10. Kaplan A, Powell J (2010) Laser welding: the spatter map. In: Proceedings of ICALEO, pp. 683–690
11. Kägeler C, Schmidt M (2010) Frequency Analysis of Frequency-based analysis of weld pool dynamics and keyhole oscillations at laser beam welding of galvanized steel sheets, Proceedings of the LANE, Part 2, pp. 447–453
12. Cai H, Xiao R (2011) Comparison of spatter characteristics in fiber and CO$_2$ laser beam welding of aluminium alloy. In: Proceeding of ICALEO, 150–158
13. Erhardt KM, Heine A, Pommersberger H (1993) Laser in der Materialbearbeitung. Vogel Buchverlag, Laser in material processing
14. Geiger M, Leitz K-H, Koch H, Otto A (2009) A 3D transient model of keyhole and melt pool dynamics in laser beam welding applied to the joining of zinc coated sheets. In: Production Engineering - Research and Development 3, 127–136
15. Otto A, Schmidt M (2010) Towards a universal numerical simulation model for laser material processing, Proceedings of the LANE, 35–46
16. Brandes EA (1992) Smithells metals reference book, 6th edn. Butterworth Publishers, Stoneham
17. Schmidt P (1894) Zerstäuben von Flüssigkeiten, Übersichtsvortrag Universität Essen, 1984. Disintegration of liquids, survey lecture, University of Essen
18. Kolmogorov et al (2001) Computing visual correspondence with occlusions using graph cuts, Proceedings of the International Conference On Computer Vision, Vancouver